

SYNTHESIS IMAGING OF THE DR 21(OH) CLUSTER. I. DUST CONTINUUM AND C¹⁸O EMISSION

JEFFREY G. MANGUM¹

Department of Astronomy, University of Texas, Austin, TX 78712, and National Radio Astronomy Observatory²

ALWYN WOOTTEN

National Radio Astronomy Observatory,² Edgemont Road, Charlottesville, VA 22903

AND

LEE G. MUNDY

Astronomy Program, University of Maryland, College Park, MD 20742

Received 1990 June 15; accepted 1991 March 26

ABSTRACT

Maps at 7'' resolution of 2.7 mm continuum and $J = 1 \rightarrow 0$ C¹⁸O emission have been made of the DR 21(OH) molecular cloud core. Three compact regions, all of which appear to be actively forming stars, have been detected. Two components, each measuring $\sim 12,000$ AU in size, containing ~ 400 – $500 M_{\odot}$ of material and encompassing H₂O masers, dominate the most compact, luminous, and massive region. Even though these two components are separated by only $\sim 8''$ on the sky and ~ 3.5 km s⁻¹ in velocity, they are quite different, possibly representing different phases of early stellar formation. The other two compact regions, mapped for the first time in molecular emission, are located to the south of the OH source, measure $\sim 30,000$ AU in size, comprise $\sim 500 M_{\odot}$ of material, and have no associated maser or known mid-infrared sources. These latter regions are warm ($T_{\text{K}} \gtrsim 20$ K) gas condensations which may have more recently evolved into their star-formation stages, as they must contain some internal heat sources which have yet to be detected.

Subject headings: interstellar: molecules — nebulae: H II regions — nebulae: individual (DR 21(OH))

1. INTRODUCTION

The W75 region of the Cygnus X H II complex is one of the most extensively studied star-forming regions in the Galaxy. W75 includes DR 21, which is an intense compact infrared and radio continuum source (Downes & Rinehart 1966; Harris 1973) and contains one of the most energetic stellar outflows known (Lane et al. 1990; Garden et al. 1986; Fischer et al. 1985). Located $\sim 3'$ north of DR 21 is a region of dense molecular material designated DR 21(OH) [also referred to as W75S or W75S(OH)]. Unlike DR 21, DR 21(OH) contains no known centimeter continuum sources, and therefore appears to be in an earlier state of evolution.

Molecular line (Genzel & Downes 1977; Wootten, Snell, & Evans 1980; Richardson et al. 1986, 1988), far-infrared (Wynn-Williams, Becklin, & Neugebauer 1974; Thum & Lemke 1975; Harvey, Campbell, & Hoffmann 1977; Harvey et al. 1986), submillimeter (Gear et al. 1988; Richardson, Sandell, & Krisciunas 1989), and millimeter (Werner et al. 1975) continuum studies have also shown that the DR 21(OH) region contains one nearby young B star [W75(IRS 1)] and at least one dense [$n(\text{H}_2) \gtrsim 10^6$ cm⁻³], warm ($T_{\text{K}} \gtrsim 30$ K) cloud core with a total mass of $\gtrsim 10^3 M_{\odot}$. These studies have shown that there are at least two embedded luminosity sources in the core. High spatial resolution ($\theta_B \simeq 3''$) observations of the 1.4 mm continuum (Woody et al. 1989) and $J = 2 \rightarrow 1$ C¹⁸O (Padin et al. 1989) emission have defined the detailed structure in one of these embedded luminosity sources. Since previous studies were either done at low spatial resolution ($\theta_B \gtrsim 15''$), or

covered only part of the region, we have made high-resolution observations of a 1.0×1.5 square arcminute section of the DR 21(OH) molecular core in order to better characterize the density, temperature, and velocity structure in this active star-forming region.

2. OBSERVATIONS

The 2.7 mm continuum and $J = 1 \rightarrow 0$ C¹⁸O emission from the DR 21(OH) molecular cloud were observed with the Owens Valley Radio Observatory (OVRO) Millimeter-Wave Interferometer during 1988 February, April, and May. Two pointing centers were used for the observations; one at $\alpha(1950) = 20^{\text{h}}37^{\text{m}}14^{\text{s}}.2$, $\delta(1950) = 42^{\circ}12'10''$ and a second at $\alpha(1950) = 20^{\text{h}}37^{\text{m}}14^{\text{s}}.6$, $\delta(1950) = 42^{\circ}11'35''$. The primary beam size was 1.2 (FWHM). Five configurations of the three-element array, with physical baselines ranging from 20 to 60 m north-south and from 15 to 60 m east-west, were used to construct 6.9×7.7 resolution maps toward the two pointing centers. The point source 2005+403 was used as a phase calibrator. The absolute flux scale was determined for each configuration from observations of Mars ($T_{\text{B}} \sim 207$ K) obtained during each track. The positional uncertainty in the maps is estimated to be $\pm 1''$. The estimated uncertainty in the absolute flux scale is 20%.

The C¹⁸O line data were obtained using thirty-two 1 MHz (2.73 km s⁻¹) and thirty-two 50 kHz (0.14 km s⁻¹) filters centered at a rest frequency of 109.782182 GHz and a V_{LSR} of -6.8 km s⁻¹. The continuum observations, obtained simultaneously with the line observations, had a bandwidth of 350 MHz. The line emission is estimated to contribute ~ 4 mJy beam⁻¹ of flux to the continuum channel, which is less than the rms noise in the final continuum maps. This negligible contribution to the continuum flux was not subtracted.

¹ National Radio Astronomy Observatory Junior Research Associate.

² The National Radio Astronomy Observatory is operated by Associated Universities, Inc., under cooperative agreement with the National Science Foundation.

Maps of the emission were made using the CLEAN algorithm in AIPS. To increase signal-to-noise in our 50 kHz data, we smoothed the data to an effective velocity resolution of 100 kHz (0.27 km s^{-1}) and applied a $u-v$ taper of $15 \text{ k}\lambda$, which yielded a spatial resolution of $9''.9 \times 9''.1$. The individual field maps were then transformed to a common phase center, corrected for the primary beam response, and averaged using the AIPS task LTESS. The rms noise levels in the continuum, 1 MHz, and 100 kHz channel maps were 8 , 100 , and $300 \text{ mJy beam}^{-1}$, respectively.

3. RESULTS

3.1. 2.7 mm Continuum Emission

Continuum emission at $\lambda = 2.7 \text{ mm}$ was detected from three distinct locations in the DR 21(OH) region (Fig. 1). We will refer to these as (clockwise from the OH maser position) DR 21(OH) main, DR 21(OH)W, and DR 21(OH)S. The source associated with the OH maser, DR 21(OH) main, appears to have two components. These components were first detected in interferometric observations of 1.4 mm continuum (Woody et al. 1989) and $J = 2 \rightarrow 1 \text{ C}^{18}\text{O}$ (Padin et al. 1989) emission. The two-component structure is also apparent in our 2.7 mm continuum (Fig. 1) and $J = 1 \rightarrow 0 \text{ C}^{18}\text{O}$ (Fig. 2) maps. Woody et al. (1989) designated the two sources MM 1 and MM 2, which is the nomenclature we will also adopt. The peak flux in Figure 1, which occurs at the OH maser position, is $193 \text{ mJy beam}^{-1}$, corresponding to a peak brightness temperature of 0.4 K . For a dust temperature of 36 K (Harvey et al. 1986), a peak brightness temperature of 0.4 K corresponds to an optical depth of 0.01 , averaged over the beam. The position centroid, FWHM size, position angle, and total flux density for each source as determined from Gaussian fits are given in Table 1.

3.2. $J = 1 \rightarrow 0 \text{ C}^{18}\text{O}$ Emission

Figures 2 and 3 present $J = 1 \rightarrow 0 \text{ C}^{18}\text{O}$ line emission maps of the DR 21(OH) region. We have detected emission in the velocity range 1.4 to -7.0 km s^{-1} , which, when compared to a single antenna spectrum obtained at the NRAO 12 m telescope toward the same pointing center, corresponds roughly to the full single-antenna line width (see Fig. 6). Figure 3, which shows line channel maps from our high-velocity resolution ($\Delta V = 0.27 \text{ km s}^{-1}$) data set, represents approximately half of the single antenna line width (due to filter bank limitations, we could observe only about half of the line). Figure 4 shows the integrated emission over the full observed range of velocity. Note that the same emission regions seen in our 2.7 mm continuum map are apparent. In Figure 5 we show the integrated emission over velocity ranges corresponding to MM 1 and MM 2, which highlights the two component structure in DR 21(OH) main.

The total integrated flux over the line components at the northern pointing center is $\sim 59 \text{ Jy km s}^{-1}$. The integrated flux

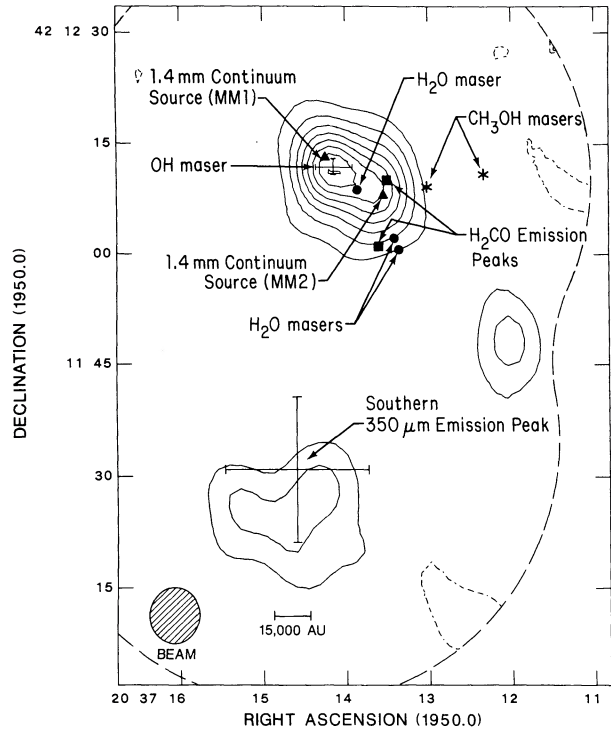


FIG. 1.—2.7 mm continuum from DR 21(OH). The contours are $-3, 3, 6, 9, 12, 15, 18, 21,$ and 24 times the rms noise of 8 mJy beam^{-1} . The beam size and linear scale are shown. The dashed curve encloses the region where the primary beam response is $\geq 50\%$. Positions of the CH_3OH (Batra & Menten 1988), H_2O (Mangum, Wootten, & Mundy 1991), and OH (Norris et al. 1982) masers and the 1.4 mm continuum (Woody et al. 1989), $2_{11} \rightarrow 2_{12} \text{ H}_2\text{CO}$ (Johnston, Henkel, & Wilson 1984), and southern $350 \mu\text{m}$ continuum (Gear et al. 1988) emission peaks are indicated. Note that the position of the northern $350 \mu\text{m}$ source, which lies near the OH maser position, is not indicated to preserve clarity.

detected in our NRAO 12 m spectrum at the same pointing center (Fig. 6) is $\sim 940 \text{ Jy km s}^{-1}$. Therefore, the interferometer maps recover $\sim 6\%$ of the single antenna flux.

4. ANALYSIS

4.1. DR 21(OH) Main

Observations of the continuum emission at millimeter and submillimeter wavelengths are useful probes of the dense molecular cloud cores because the emission is usually optically thin. Assuming that this continuum emission arises from dust grains, the emission spectrum for a compact object is given by

$$S_\nu = \frac{2h\nu^3\Omega_S}{c^2} \left\{ \frac{1 - \exp[-\tau_0(\nu/\nu_0)^\beta]}{[\exp(h\nu/kT_D) - 1]} \right\}, \quad (1)$$

where Ω_S is the source solid angle, τ_0 is the optical depth at

TABLE 1
2.72 MM CONTINUUM COMPONENT CHARACTERISTICS

Component	$\alpha(1950)$	$\delta(1950)$	$\theta_{\text{maj}} \times \theta_{\text{min}}$	Position Angle	Integrated Flux (Jy)
MM 1	$20^{\text{h}}37^{\text{m}}14.^{\text{s}}2$	$42^{\circ}12'12''$	$7''.8 \times <7''$	13°	0.269
MM 2	$20\ 37\ 13.6$	$42\ 12\ 09$	$8.7 \times <7$	8	0.217
DR 21(OH)W	$20\ 37\ 12.0$	$42\ 11\ 48$	$9.3 \times <7$	7	0.097
DR 21(OH)S	$20\ 37\ 14.7$	$42\ 11\ 25$	18.8×11.3	100	0.318

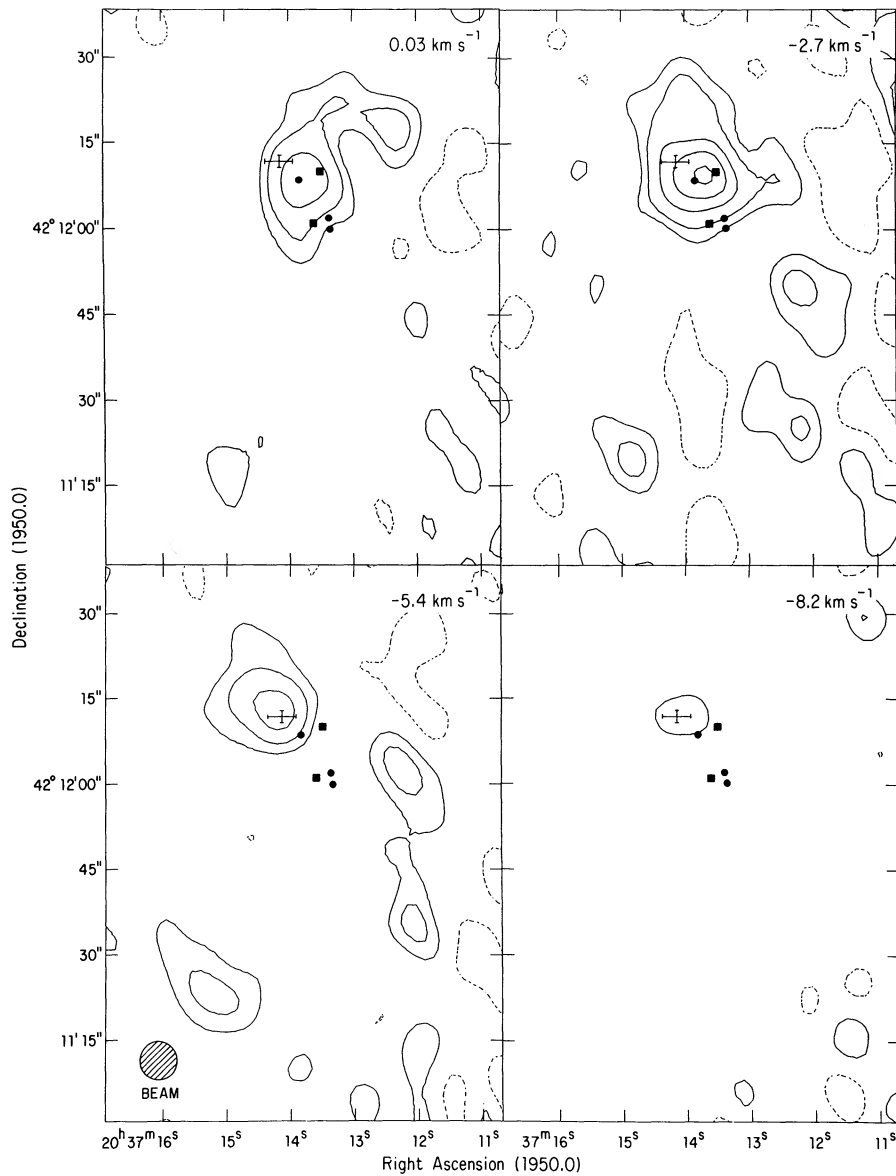


FIG. 2.—Maps of the $J = 1 \rightarrow 0$ $C^{18}O$ emission from our low-velocity resolution ($\Delta V = 2.7 \text{ km s}^{-1}$) observations of DR 21(OH). Contours are $-3, 3, 6, 12, 18,$ and 24 times the rms noise of $100 \text{ mJy beam}^{-1}$ ($-0.6, 0.6, 1.2, 2.4, 3.6,$ and 4.8 K). The beam size and LSR velocity for each channel are indicated. Positions of the H_2O (circles) and OH (small cross) masers as well as the $2_{11} \rightarrow 2_{12}$ H_2CO emission peaks (squares) are indicated as in Fig. 1.

frequency ν_0 , β is the dust emissivity power law, and T_D is the dust temperature. The source is assumed to be a disk with uniform optical depth and temperature. In more convenient units, this equation becomes

$$S_\nu(\text{Jy}) = 0.73 \frac{\theta_s^2(\text{''})}{\lambda^3(\text{mm})} \left[\frac{1 - \exp\{-\tau_{250}[0.25/\lambda(\text{mm})]^\beta\}}{\exp\{14.39/[\lambda(\text{mm})T_D(\text{K})]\} - 1} \right], \quad (2)$$

where we have assumed that $\Omega_s = \pi(\theta_s/2)^2$, where θ_s is the source angular diameter, and τ_{250} is the optical depth at $250 \mu\text{m}$.

In Figure 7 we plot the available dust continuum measurements of DR 21(OH) main at wavelengths $\geq 50 \mu\text{m}$. We exclude the $20 \mu\text{m}$ measurement of Harvey et al. (1986) because it was a single-point measurement obtained at relatively high spatial resolution ($\theta_B = 7''.5$) and is therefore sensitive to only a

small portion of the DR 21(OH) main source. Most of the measurements shown in Figure 7 were obtained with beam sizes $\geq 15''$ so that MM 1 and MM 2 remain unresolved. For the measurements at $50, 100, 350, 800,$ and $1100 \mu\text{m}$, we have plotted the peak flux from the DR 21(OH) main region. The measurements at 1.4 and 2.7 mm are the integrated emission over MM 1 and MM 2. Since the resolution at which the single antenna measurements when made ($\theta_B \approx 15''$) is approximately equal to the measured source sizes at 2.7 mm , and since the sizes of centrally heated sources of dust continuum emission should decrease at shorter wavelengths, a direct comparison of single antenna flux measurements with the integrated emission at 1.4 and 2.7 mm should be valid. By fixing the source size at $10''$ (as measured in our 2.7 mm continuum observations), allowing the dust emissivity power law β to vary between 1 and 2 (Day 1976; Koike, Hasegawa, & Manabe 1980; Tielens & Allamandola 1987), and iterating on τ_{250} and T_D , we have

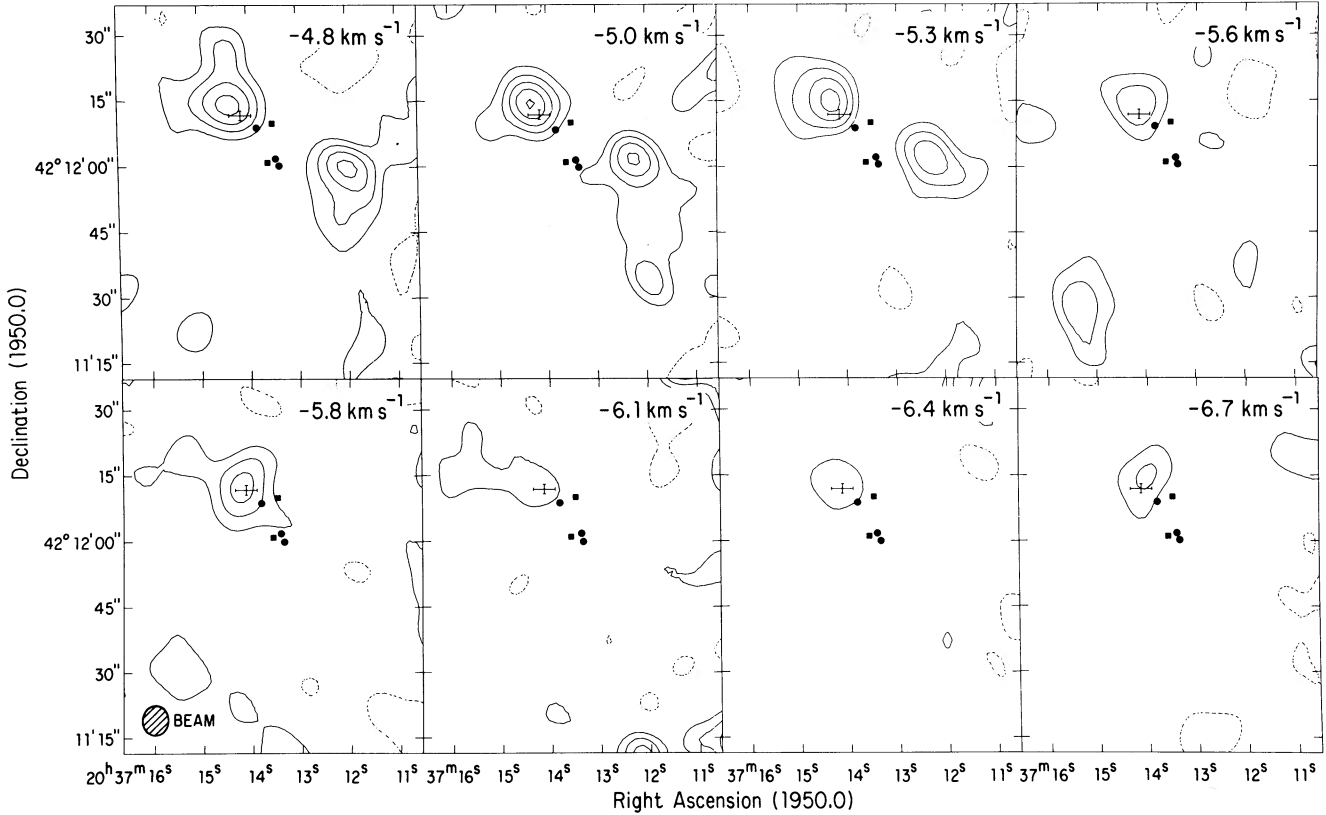


FIG. 3.—Maps of the $J = 1 \rightarrow 0$ $C^{18}O$ emission from our high-velocity resolution ($\Delta V = 0.27 \text{ km s}^{-1}$) observations of DR 21(OH). Contours are $-3, 3, 5, 7, 9,$ and 11 times the rms noise of $300 \text{ mJy beam}^{-1}$ ($-1.0, 1.0, 1.7, 2.3, 3.0,$ and 3.6 K). The beam size and LSR velocity for each channel are indicated. Positions of the H_2O (circles) and OH (small cross) masers as well as the $2_{11} \rightarrow 2_{12}$ H_2CO emission peaks (squares) are given as in Fig. 1.

obtained fits of equation (2) to the dust continuum measurements from $50 \mu\text{m}$ to 2.7 mm . The best fits are obtained for $T_D = 42 \pm 3 \text{ K}$, $\tau_{250} = 1.0 \pm 0.4$, and $\beta = 1.7 \pm 0.3$. The error bars here are formal errors on the fit and do not include systematic errors due to temperature and opacity gradients in the source. With this information we can calculate the peak hydrogen column density $N(H + H_2)$, the peak beam-averaged density $n(H + H_2)$, and the total mass M_{TOT} :

$$N(H + H_2) = 7.0 \times 10^{24} \left[\frac{\lambda(\text{mm})}{0.4} \right]^\beta \tau_\lambda \text{ cm}^{-2}, \quad (3)$$

$$n(H + H_2) = 6.3 \times 10^{-17} \frac{N(H + H_2)}{\theta_s(\text{''})D(\text{kpc})} \text{ cm}^{-3}, \quad (4)$$

and

$$M_{\text{TOT}} = 0.02D^2(\text{kpc})S_\nu(\text{Jy}) \left[\frac{\lambda(\text{mm})}{0.25} \right]^{\beta+3} \times \left\{ \exp \left[\frac{14.4}{\lambda(\text{mm})T_D(\text{K})} \right] - 1 \right\} M_\odot, \quad (5)$$

where we have used an $N(H + H_2)$ to τ_{400} conversion factor of 7×10^{24} (Hildebrand 1983). Assuming a spherical source and $D = 3 \text{ kpc}$ (Campbell et al. 1982), $N(H + H_2) \approx 3 \times 10^{24} \text{ cm}^{-2}$, $n(H + H_2) \approx 6 \times 10^6 \text{ cm}^{-3}$, and $M_{\text{TOT}} \approx 860 M_\odot$ in DR 21(OH) main. Note that our direct estimate of the 2.7 mm optical depth of 0.01 (§ 3.1) yields a peak $N(H + H_2) = 1.9$

$\times 10^{24} \text{ cm}^{-2}$, consistent with the result above. As Hildebrand (1983) notes, these calculations are uncertain to factors of 3–5.

Single antenna measurements of the dust continuum emission at 350 and $800 \mu\text{m}$ yield a total mass in the range $(3\text{--}5) \times 10^3 M_\odot$ and a source size $\gtrsim 15''$ (Gear et al. 1988; Richardson et al. 1989). Therefore, much of the integrated flux measured at these wavelengths is produced by weak extended ($\theta_s \gtrsim 30''$) emission to which our interferometric measurements are not sensitive.

To calculate the total mass using our $C^{18}O$ measurements we use the relationship between the integrated flux from an optically thin molecular transition and the total number of molecules

$$\int S_\nu dV = \frac{16\pi^3 |\mu_{J_I J_u}|^2 v^3}{3c^2 D^2 g_J} \left(\frac{g_J g_K g_I}{Q_{\text{ROT}}} \right) \mathcal{N} \exp\left(-\frac{E_u}{T_{\text{ex}}}\right), \quad (6)$$

where $|\mu_{J_I J_u}|^2$ is the molecular dipole moment matrix element, g_J and g_K are rotational degeneracies, g_I is the nuclear spin degeneracy, D is the distance to the source, \mathcal{N} is the total number of molecules, and the other symbols have their usual meanings. For $C^{18}O$, $|\mu_{J_I J_u}|^2 = \mu^2 J_u$, $\mu = 0.1098 \text{ Debye}$ (Chakerian & Tipping 1983), $g_J = 2J_u + 1$, $g_K = g_I = 1$, and $Q_{\text{ROT}} \approx kT_{\text{ex}}/hB_0 + \frac{1}{3} \approx 0.38(T_{\text{ex}} + 0.88)$, assuming all levels have the same T_{ex} .

Using the relationship between the total number of molecules and the mass in the beam

$$\mathcal{N} = \frac{X(C^{18}O)M_{\text{TOT}}}{\mu_m m_{H_2}},$$

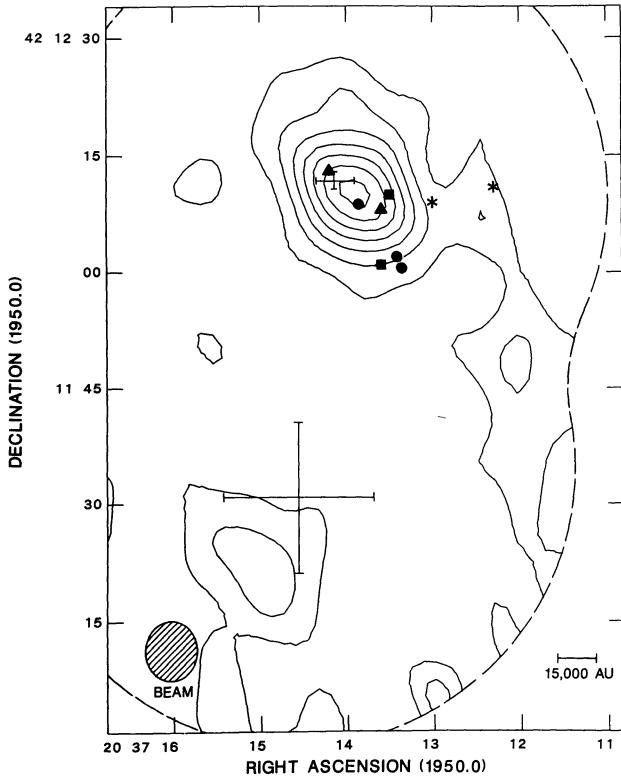


FIG. 4.—Integrated $J = 1 \rightarrow 0$ $C^{18}O$ emission from our low-velocity resolution ($\Delta V = 2.7 \text{ km s}^{-1}$) observations of DR 21(OH). Contours are 1, 3, 5, 7, 9, 11, and 13 $\text{Jy beam}^{-1} \text{ km s}^{-1}$ (2, 6, 10, 14, 18, 22, and 26 K km s^{-1}). The beam size, linear scale, and the positions of the H_2O (circles), OH (small cross), and CH_3OH (asterisks) masers and 1.4 mm continuum (triangles), $2_{11} \rightarrow 2_{12}$ H_2CO (squares), and southern $350 \mu\text{m}$ continuum (large cross) emission peaks are indicated as in Fig. 1. The dashed curve encloses the region where the primary beam response is $\geq 50\%$.

where $X(C^{18}O)$ is the abundance of $C^{18}O$ relative to H_2 and μ_m is the reduced mass for hydrogen ($= 1.36$), we find that

$$M_{\text{TOT}}(M_{\odot}) = 3.7 \times 10^{-3} \frac{(T_{\text{ex}} + 0.88)D^2(\text{kpc})}{J_u v^3(\text{GHz})X(C^{18}O)} \times \exp\left(\frac{E_u}{T_{\text{ex}}}\right) \int S_{\nu} dV(\text{Jy km s}^{-1}). \quad (7)$$

For the $J = 1 \rightarrow 0$ transition of $C^{18}O$, this equation becomes

$$M_{\text{TOT}}(M_{\odot}) = 0.014(T_{\text{ex}} + 0.88)D^2(\text{kpc}) \left[\frac{2 \times 10^{-7}}{X(C^{18}O)} \right] \times \exp\left(\frac{5.27}{T_{\text{ex}}}\right) \int S_{\nu} dV(\text{Jy km s}^{-1}). \quad (8)$$

Assuming $T_{\text{ex}} = T_D = 42 \text{ K}$ and $X(C^{18}O) = 2 \times 10^{-7}$ (Frerking, Langer, & Wilson 1982), we calculate $M_{\text{TOT}} \approx 236 M_{\odot}$ for DR 21(OH) main using our $J = 1 \rightarrow 0$ $C^{18}O$ measurements.

Note that this measurement of M_{TOT} is $\sim \frac{1}{3}$ that derived from our 2.7 mm continuum observations. Even though this discrepancy is within the uncertainties of both mass calculations, it is instructive to comment on the possible reasons for this difference. The simplest explanation for this discrepancy would be our assumption that the $J = 1 \rightarrow 0$ $C^{18}O$ transition is optically thin. To test this assumption, we compare our measurements of $T_B(J = 1 \rightarrow 0)$ with interferometric measurements

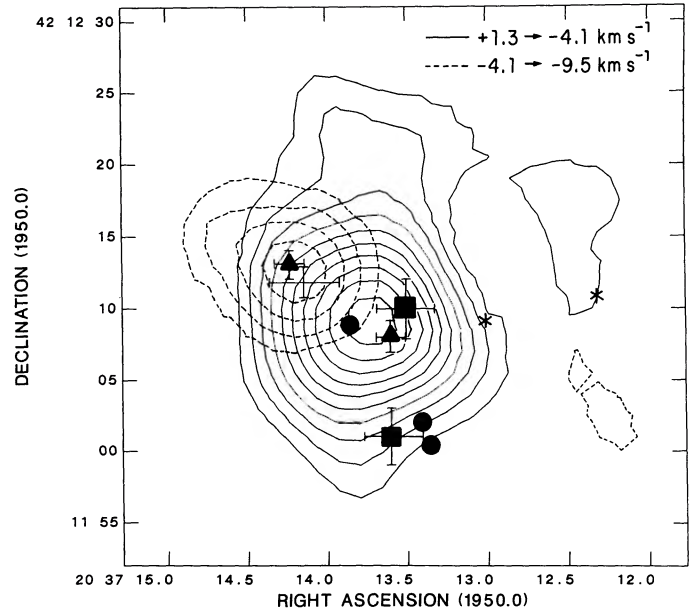


FIG. 5.—Integrated $J = 1 \rightarrow 0$ $C^{18}O$ emission from our low-velocity resolution ($\Delta V = 2.7 \text{ km s}^{-1}$) observations of DR 21(OH) over the LSR velocity ranges of 1.3 to -4.1 km s^{-1} (solid contours) and -4.1 to -9.5 km s^{-1} (dashed contours). These two condensations correspond to the 1.4 mm continuum emission peaks MM 2 and MM 1, respectively. Contour intervals are 2, 3, 4, 5, 6, 7, 8, 9, 10, and 11 $\text{Jy beam}^{-1} \text{ km s}^{-1}$ (4, 6, 8, 10, 12, 14, 16, 18, 20, and 22 K km s^{-1}). Positions of the H_2O (circles), OH (cross), and CH_3OH (asterisks) masers and 1.4 mm continuum (triangles) and $2_{11} \rightarrow 2_{12}$ H_2CO (squares) emission peaks are given as in Figure 1. Positional error bars for each measurement are indicated (the errors on the H_2O and CH_3OH maser positions are smaller than the symbols marking their positions).

of the $J = 2 \rightarrow 1$ transition toward DR 21(OH) main. $T_B(J = 1 \rightarrow 0) = 5.0 \pm 1.2 \text{ K}$ in a $6''.9 \times 7''.7$ beam (the peak in our low-velocity resolution channel maps) and $T_B(J = 2 \rightarrow 1) = 13 \pm 4.9 \text{ K}$ in a $6''.8 \times 3''.4$ beam (Padin et al. 1989). The errors on these measurements include the 20% and 30% absolute flux calibration uncertainties at 2.7 and 1.4 mm, respectively. Since the emission in the smaller $J = 2 \rightarrow 1$ beam appears to be only marginally resolved, after scaling the $J = 2 \rightarrow 1$ brightness temperature by the ratio of the beam areas (a factor of 0.44), we find that $[T_B(J = 1 \rightarrow 0)]/[T_B(J = 2 \rightarrow 1)] = 0.86 \pm 0.39$, suggesting that $\tau(J = 1 \rightarrow 0) \gtrsim 0.5$. Therefore, the total $C^{18}O$ column densities and the total masses calculated using our $J = 1 \rightarrow 0$ measurements are likely to be lower limits. A moderate optical depth of ~ 3 could bring the two mass estimates into agreement. This difference in the calculated mass might also be explained by a $C^{18}O$ abundance smaller than our assumed value of 2×10^{-7} , which is based on $C^{18}O$ measurements in ρ Oph and Taurus (Frerking et al. 1982) at $A_V < 21$ mag. It is possible that $C^{18}O$ is depleted in the dense, more opaque regions of DR 21(OH). For a standard collision rate of $6 \times 10^{-11} \text{ cm}^3 \text{ s}^{-1}$ and unit sticking probability, the depletion time scale is $\sim (3 \times 10^9)/n(H_2)$ yr. Therefore, significant depletion could take place in $\lesssim 500$ yr for $n(H_2) \gtrsim 6 \times 10^6 \text{ cm}^{-3}$.

The sources MM 1 and MM 2, though separated by only $8''$ ($24,000 \text{ AU}$ at a distance of 3 kpc) appear to be quite different objects. Below we describe each source and identify its possible evolutionary state.

4.1.1. MM 1

As Figure 1 indicates, MM 1 has an OH maser located within $1''$ of its center and H_2O maser emission on its south-

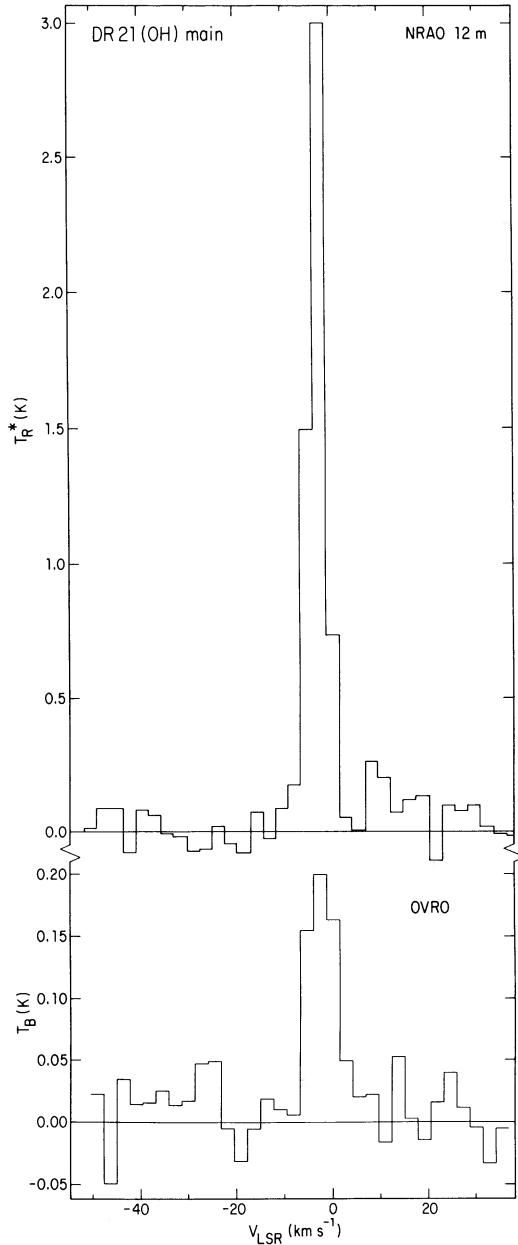


FIG. 6.—Comparison between interferometric and single antenna spectra of $J = 1 \rightarrow 0$ $C^{18}O$ emission toward DR 21(OH). The interferometer spectrum was produced by integrating over the primary beam of the observations (1.2) in each channel of our low-velocity resolution ($\Delta V = 2.7 \text{ km s}^{-1}$) data set. The single antenna spectrum was obtained at the NRAO 12 m telescope, where $\theta_B \approx 1'$ and $\Delta V = 2.7 \text{ km s}^{-1}$.

western periphery. In $20 \mu\text{m}$ continuum emission, MM 1 coincides with the southwestern component of a double source with a component separation of $6''$ (Genzel 1989). We identify this $20 \mu\text{m}$ object as the embedded heating source for the dust. The northeastern $20 \mu\text{m}$ source has no observed molecular spectral line or millimeter/submillimeter dust continuum emission but lies along the same axis as MM 1 and MM 2. This suggests that this object has emerged from the gas and dust which still encompasses MM 1 and MM 2. As it is the warmest compact source in the region (see below), MM 1 is most likely the source of the NH_3 (5,5) and (7,7) emission observed

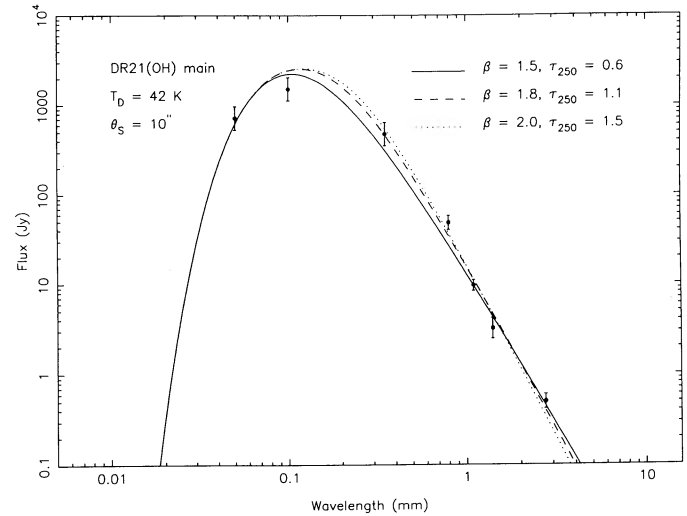


FIG. 7.—Dust emission distribution for the DR 21(OH) main region. For a dust temperature of 42 K and a source diameter of $10''$, each curve represents a modified blackbody with an emissivity (β) and optical depth at $250 \mu\text{m}$ (τ_{250}) listed in the upper right. The flux measurements used were drawn from the following references: 50 and $100 \mu\text{m}$, Harvey et al. (1986); 350 μm , Gear et al. (1988); 800 and $1100 \mu\text{m}$, Richardson, Sandell, & Krisciunas (1989); 2.7 mm, this work; 1.4 mm, Woody et al. (1989).

toward this region (Mauersberger et al. 1985, 1986). No 2 cm (Johnston, Henkel, & Wilson 1984) continuum emission has been detected to a limit of 10 mJy beam^{-1} toward this source. Therefore, MM 1 appears to contain at least one massive pre-main-sequence star which remains deeply embedded.

Tables 1 and 2 list our determinations of the physical parameters for MM 1. The positions of the $J = 1 \rightarrow 0$ $C^{18}O$ and 2.7 mm continuum components correspond to within $2''$ with those observed in the $C^{18}O$ $J = 2 \rightarrow 1$ transition (Padin et al. 1989) and 1.4 mm continuum (Woody et al. 1989). Since MM 1 is the warmest compact source in the region, it is the likely source of the 50 and $100 \mu\text{m}$ emission. From our dust model fits to the entire DR 21(OH) main source (§ 4.1), we found that $\beta = 1.7 \pm 0.3$. In the dust model fits to the MM 1 and MM 2 components of DR 21(OH) main, we will assume that the dust emission properties are the same and that $\beta = 1.7$.

We have made fits of equation (2) to the 2.7 mm, 1.4 mm, 100 μm , and 20 μm measurements of MM 1, setting $\beta = 1.7$, $\theta_S = 4''$ (from the 1.4 mm continuum measurements of Woody et al. 1989), and iterating on τ_{250} and T_D . We use the peak flux from the 100, 50, and 20 μm measurements (Harvey et al. 1986) and the integrated flux from MM 1 in the 2.7 (this work) and 1.4 mm (Woody et al. 1989) interferometer maps. Flux measurements at 350, 800, and $1100 \mu\text{m}$ have not been included in these fits because they do not distinguish between the MM 1 and MM 2 components. The best fit for MM 1 is plotted in Figure 8 and listed in Table 3. Note that the flux measurements plotted at 2.7 and 1.4 mm in Figure 8 represent the total integrated flux from MM 1 and MM 2 combined and that each source makes approximately equal contributions to these total fluxes. The derived bolometric luminosity of MM 1 is $1.7 \times 10^4 L_\odot$, which corresponds to a B0.5 V zero-age main-sequence star (Panagia 1973).

4.1.2. MM 2

The source MM 2 is located $\sim 8''$ southwest of MM 1. As with MM 1, H_2O maser emission is found on the southwestern

TABLE 2
 $J = 1 \rightarrow 0$ C¹⁸O COMPONENT CHARACTERISTICS

Component	$\alpha(1950)^a$	$\delta(1950)^a$	$\theta_{\text{maj}} \times \theta_{\text{min}}^a$	$\int S_\nu dV^a$ (Jy km s ⁻¹)	FWZI (km s ⁻¹)	$N_{\text{TOT}}(\text{C}^{18}\text{O})^b$ (10 ¹⁶ cm ⁻²)	$M_{\text{TOT}}^{b,c}$ (M_\odot)
MM 1	20 ^h 37 ^m 14 ^s .2	42°21'13"	9".1 × <7"	10.3	5.4 ^d	3.0	85
MM 2	20 37 13.8	42 12 09	10.1 × 8.4	28.3	5.4 ^d	3.4	130
DR 21(OH)W ^e	20 37 12.0	42 11 48	~20 × 10	~15	~8.2	~0.7	~70
DR 21(OH)S	20 37 15.0	42 11 21	13.7 × <7	13.6	8.2	1.3	65

^a Except for DR 21(OH)W, obtained from Gaussian fit to component in wide channel ($\Delta V = 2.73$ km s⁻¹) maps.

^b Due to the assumption that $\tau(J = 1 \rightarrow 0) \ll 1$, these are likely to be lower limits (see § 4.1).

^c Assuming $X(\text{C}^{18}\text{O}) = 2 \times 10^{-7}$ and $T_{\text{ex}} = T_D$ (see Table 3).

^d Note that the FWZI for DR 21(OH) main (MM 1 and MM 2 combined) is 10.8 km s⁻¹.

^e Source not well represented by a Gaussian. Values given were measured directly from integrated intensity maps.

portion of MM 2 (see Fig. 1). Harvey et al. (1986) made a 20 μm map of the region containing MM 2 and detected no sources to a level of 3 Jy in a 7".5 beam; MM 2 lies beyond the region mapped by Genzel (1989). Therefore, MM 2 has no known 20 μm emission. Tables 1 and 2 list the relevant 2.7 mm continuum and $J = 1 \rightarrow 0$ C¹⁸O derived parameters for MM 2.

Resolved measurements of the dust continuum flux from MM 2 exist only at 1.4 and 2.7 mm. Since we have more information about the dust continuum emission from MM 1 plus MM 2 [DR 21(OH) main] and we have obtained a reliable model fit to MM 1 (see § 4.1.1), we have used the combined source information to determine the source properties for MM 2. The upper limit from the Harvey et al. (1986) map restricts the dust temperature to lie below 55 K. The dust temperature for the combined source [$T_D = 36$ K, Harvey et al. (1986)] lies below the best fit to MM 1. Using newly available fluxes, we found $T_D = 42$ K for the combined source from the fit in Figure 7 (see § 4.1). As MM 2 is fainter than MM 1 at *all* wavelengths, its luminosity must be lower; we find an upper limit of $L_{\text{BOL}} < 1.3 \times 10^4 L_\odot$ for MM 2. A high-resolution multitransition NH₃ study (Mangum, Wootten, & Mundy 1991) suggests the temperature of the gas associated with MM 2 is ~30 K. By setting $\beta = 1.7$ (see § 4.1), $\theta_s = 4''$ (from the 1.4 mm continuum measurements of Woody et al. 1989), and $T_D = 30$ K (Mangum et al. 1991), the only free parameter in the model for MM 2 is τ_{250} . The best fit of equation (2) for MM 2 (and MM 1 + MM 2) suggests that $\tau_{250} \sim 4$. This model is plotted in Figure 8 and its parameters listed, along with calculations of $N(\text{H} + \text{H}_2)$, $n(\text{H} + \text{H}_2)$, and M_{TOT} using equations (3), (4), and (5), in Table 3. Since the luminosity of MM 2 must exceed $10^3 L_\odot$ for these model parameters and less than a third of this can originate from heating by MM 1, MM 2 must contain an independent source of luminosity. If this source is a main-sequence star, the limits on luminosity constrain the stellar mass to between 6 and 15 M_\odot , an early B star.

4.2. DR 21(OH)W

In Figures 1 and 4 there is a continuum and line feature situated to the southwest of DR 21(OH) main. Tables 1 and 2 list its measured physical parameters (note that these parameters are somewhat uncertain because DR 21(OH)W is located near the half-power point of our primary beam). Although not completely encompassed by the narrow filter bank C¹⁸O observations, the source V_{LSR} lies near -4.9 km s⁻¹, unambiguously establishing its kinematic association with the DR 21(OH) complex. Extended north-south, this source also appears as a connecting bridge of C¹⁸O (Fig. 4) emission between DR 21(OH) main and DR 21(OH)S.

Since measurements of resolved dust continuum emission from DR 21(OH)W exist only at three wavelengths, equation (2) cannot be used to derive accurate dust emission properties. However, the maps of Harvey et al. (1986) provide useful constraints on the existence of very warm components. Together, these data constrain the luminosity of the core. Therefore, we plot in Figure 9 the fluxes at 800 and 1100 μm (Richardson et al. 1989) along with our integrated 2.7 mm continuum flux and the Harvey et al. (1986) limits. Superposed on these measurements we show curves representing the modified blackbody emission spectrum (eq. [2]) at three representative dust temperatures for a source size of 9", assuming $\beta = 1.5$. A value of $\tau_{250} = 1.3 \pm 0.8$ was found to give the best fits to the data. Although the data are insufficient to characterize the source well, the long-wavelength points limit dust temperatures to values above ~20 K, and luminosities above $\sim 10^3 L_\odot$. The short-wavelength limits suggest upper limits to the dust temperature lie near 26 K, with luminosities near $2.5 \times 10^3 L_\odot$ —if these limits were much higher, a distinct strong source of 100 μm emission would appear in the maps made by Harvey et al. (1986). The luminosity limits are consistent with the presence of a main-sequence B2–B3 star.

TABLE 3
 COMPONENT PROPERTIES DERIVED FROM DUST MODELS

Component	θ_s (arcsec)	T_D (K)	β	τ_{250}	$N(\text{H} + \text{H}_2)$ (10 ²⁴ cm ⁻²)	$n(\text{H} + \text{H}_2)$ (10 ⁶ cm ⁻³)	M_{TOT}^a (M_\odot)	L_{BOL} (10 ³ L_\odot)
MM 1	4 ^b	58	1.7	2.5	7.9	41	350	17
MM 2	4 ^b	30 ^c	1.7	4.0	13	68	570	1.2
DR 21(OH)W ^d	9	≥ 20	1.5	~1.3	~4.5	11	≤ 250	~2.5
DR 21(OH)S ^d	17	≥ 20	1.5	~0.3	~1.0	1	≤ 810	~2.5

^a Calculated using 2.7 mm integrated flux from Table 1.

^b From measurements at 1.4 mm (Woody et al. 1989; Padin et al. 1989).

^c Value fixed by NH₃ (1, 1) and (2, 2) observations (Mangum, Wootten, & Mundy 1991).

^d Value for β is assumed.

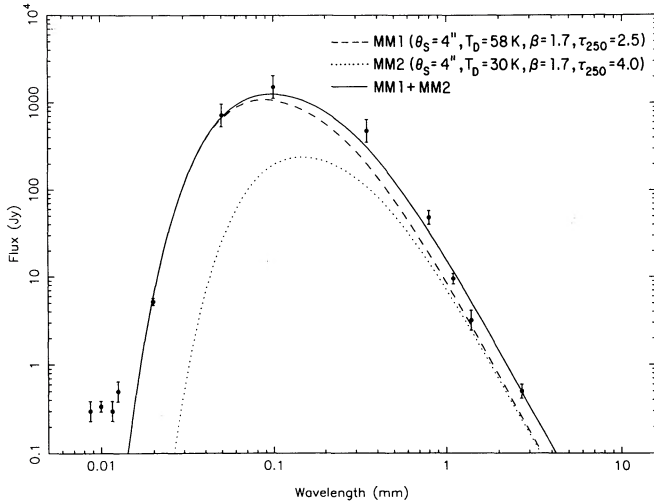


FIG. 8.—Two-component dust model for DR 21(OH) main. The flux measurements for $\lambda \leq 20 \mu\text{m}$ are from Harvey et al. (1986) while the references for the measurements at $\lambda \geq 50 \mu\text{m}$ are the same as in Fig. 7. Note that the measurements at 8.7, 10.0, 11.6, 12.5, 350, 800, and 1100 μm were not included in the model fits and are only shown for completeness. The flux measurements at 2.7 mm and 1.4 mm represent the total integrated flux from MM 1 and MM 2 (each source makes approximately equal contributions to these total fluxes). Also, the dust temperature for MM 2 (30 K) was fixed in this model calculation (see text).

In Table 3 we list calculations of $N(\text{H} + \text{H}_2)$, $n(\text{H} + \text{H}_2)$, and M_{TOT} for DR 21(OH)W using equations (3), (4), and (5). Note that because this source is extended in both the line and continuum (Richardson et al. 1989), accurate calculation of source properties is difficult. Although its high luminosity suggests it contains the equivalent of an early B star, DR 21(OH)W has no associated OH or H_2O maser emission (Norris et al. 1982; Mangum et al. 1991), nor any mid-infrared, 1.3, or 2 cm continuum emission (Harvey et al. 1986; Mangum et al. 1991; Johnston et al. 1984).

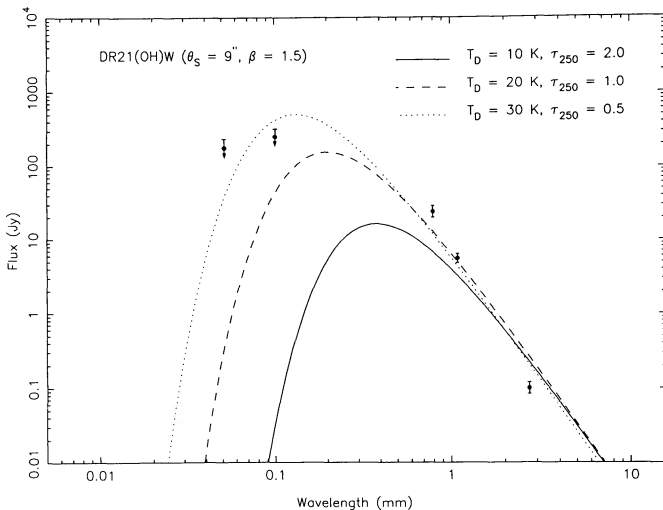


FIG. 9.—Dust emission distribution for DR 21(OH)W. Flux measurements from the same references as in Fig. 7. Representative modified blackbody curves at three values of T_D and τ_{250} for θ_s and β fixed at their indicated values are shown.

4.3. DR 21(OH)S

In Tables 1 and 2 we list the relevant physical parameters for this source as determined from our 2.7 mm and $J = 1 \rightarrow 0$ C^{18}O maps. DR 21(OH)S was first detected as a strong source of continuum emission at 350 μm (Gear et al. 1988). Its line emission lies within the confines of the narrow filter bank, allowing us to establish its kinematic association with DR 21(OH) at $V_{\text{LSR}} = -5.6 \text{ km s}^{-1}$. Note that in our line and continuum observations (see Figs. 1 through 4) DR 21(OH)S appears to be elongated in the east-west direction (this is also true of the CH_3OH maps of Batrla & Menten 1988 and the 350 μm data of Gear et al. 1988), indicating that there may be multiple components.

In Figure 10 we have plotted the available DR 21(OH)S dust continuum measurements at 50 and 100 μm (Harvey et al. 1986), 350 μm (Gear et al. 1988), 800 and 1100 μm (Richardson et al. 1989), and 2.7 mm (this work) in the same manner as was done for the other DR 21(OH) sources. We also show in Figure 10 the modified blackbody spectrum (eq. [2]) at three dust temperatures for a source size of $17''$, assuming $\beta = 1.5$. A value of $\tau_{250} = 0.3 \pm 0.2$ was found to give the best fits to the data. Again, long-wavelength fluxes constrain the temperature to lie above $\sim 20 \text{ K}$, while the 100 μm flux forces it below $\sim 23 \text{ K}$. Thus, the luminosity of the source is fairly well constrained, and must lie between $\sim 2000\text{--}3000 L_{\odot}$. Such a high luminosity requires that DR 21(OH)S, like DR 21(OH) main and DR 21(OH)W, contain at least one luminous ($\sim \text{B2}$) embedded star. Heating from several external sources, such as cosmic rays or diffuse background ultraviolet radiation, can supply only a small fraction of the observed luminosity. The nearby DR 21 and DR 21(OH) main sources can each supply about 100 solar luminosities to DR 21(OH)S, and even less if all three sources do not lie in the plane of the sky. Most likely, stars too young, too low in mass, or embedded too deeply to have been detected yet in the near- and mid-infrared supply the energy necessary to account for the core's far-infrared luminosity. Table 3 lists estimates of $N(\text{H} + \text{H}_2)$, $n(\text{H} + \text{H}_2)$, and M_{TOT} for DR 21(OH)S using equations (3), (4), and (5).

The low dust temperature, absence of H_2O and OH maser emission, and lack of mid-infrared or 2 cm radio continuum emission all suggest that star formation remains in its earliest

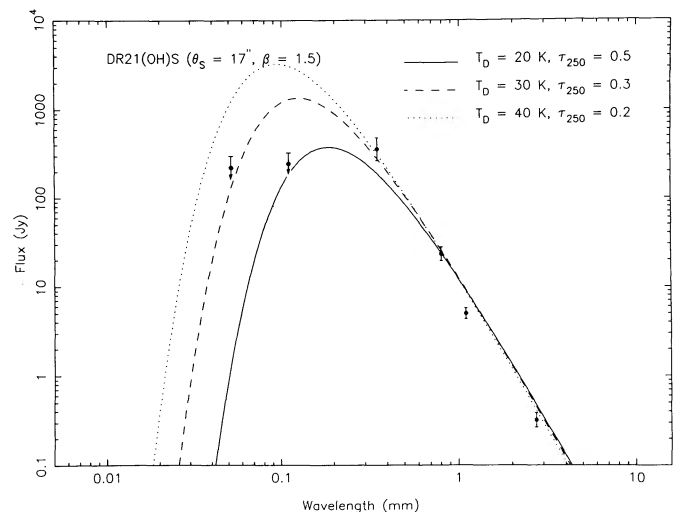


FIG. 10.—Same as Fig. 9 for DR 21(OH)S

stages in DR 21(OH)S; it may harbor a substantial population of undetected moderate mass stars.

5. THE STELLAR CONTENT OF DR 21(OH)

Our analysis of the infrared, submillimeter, and millimeter emission properties of the DR 21(OH) components suggests that massive star formation is occurring in this region. The total luminosity of the region lies between the $10^4 L_{\odot}$ of the Ophiuchus star-formation region (Wilking, Lada, & Young 1989) and that of the prototypical massive O and B star-forming region, the Kleinmann-Low (KL) nebula of the Orion molecular cloud. The total infrared flux received from the central 1' of the KL nebula corresponds to a bolometric luminosity of $10^5 L_{\odot}$ (Werner et al. 1976). The extent of the region is also intermediate between these two nearer complexes. At the distance of DR 21(OH) (3000 pc), the Ophiuchus core would extend over 0.3 by 2', while the KL nebula would subtend 10". For comparison, the size of the MM 1/MM 2 region is $\sim 10''$ (see § 4.1) while DR 21(OH)S has a measured 2.7 mm continuum size of $\sim 17''$ (see Table 3). The Ophiuchus core has produced 2 OB stars and Orion-KL at least one O star, compared to evidence for 3–4 early B stars found in DR 21(OH).

The Ophiuchus cloud provides a convenient paradigm for comparison. The 2σ sensitivity limit of our continuum map lies at an equivalent extinction of $A_v = 50$ mag, exactly the limit to which Wilking & Lada (1983) defined the Ophiuchus core. The $C^{18}O$ limits sample more of the envelope, reaching an equivalent extinction of $A_v = 25$ mag at the 2σ level. The Ophiuchus core mass ($\sim 290 M_{\odot}$; Wilking & Lada 1983) approximates the masses of the DR 21(OH) cores, but the latter tend to be more compact, and consequently average higher in density. Using the rather complete survey of the embedded stellar population of the Ophiuchus cluster as a guide, we speculate now on the character of the stellar population in the DR 21(OH) clouds.

With two mid-infrared stars identified, and including MM 2, the main region of the cloud appears to have produced the basis, at least, of a cluster. Padin et al. (1989) discussed this possibility, noting that MM 1 and MM 2 could be bound. Our more sensitive observations have detected more mass in the region. The virial limit lies below the observed mass, suggesting that the core is bound. Using the Miller & Scalzo (1979) initial mass function (IMF), one might expect a star as luminous as MM 1 ($15 M_{\odot}$) to be accompanied by $300 M_{\odot}$ of less massive stars. If the three observed objects comprise the entire stellar population, the star-forming efficiency (SFE) of the core ($\sim 3\%$) is similar to that of Taurus-like clouds (2%–9%, see review by Wilking 1989). Unlike those clouds, however, DR 21(OH) MM 1/MM 2 has formed several massive stars. One expects, then, that the star-forming efficiency will be more similar to that observed in the Ophiuchus cloud, for which Wilking et al. (1989) find SFE $\sim 22\%$. If this efficiency applies to DR 21(OH), we would expect to find a cluster of stars comprising about $230 M_{\odot}$, consistent with IMF-based expectations.

The source DR 21(OH)W appears to be somewhat less massive than its neighbors, and may not be bound. Assuming a central B3 star supplies its luminosity, some structure within the core must have been bound if the star formed there. Using a Miller-Scalo IMF to estimate the SFE for this core leads to the unappealing suggestion that its SFE exceeds 50%. However, this core is the least well-characterized of the three. It should be possible to place good constraints on the embedded stellar population through the use of IR imaging.

For DR 21(OH)S, the virial mass lies very close to the observed mass in Table 3, and we suppose the core to be in the process of the formation of a bound cluster. The luminosity of the core suggests the presence of a B2 star, for which a Miller-Scalo IMF would predict $120 M_{\odot}$ of less massive stars. Again, a SFE similar to Ophiuchus would predict a similar population of embedded stars.

The cluster of cloud cores in DR 21(OH) appears to have formed several early B stars. The arguments presented above suggest many other stars may be present. Therefore, as in the Ophiuchus molecular complex, a new stellar cluster appears to be forming in DR 21(OH).

6. CONCLUSIONS

Observations of the 2.7 mm continuum and $J = 1 \rightarrow 0 C^{18}O$ emission toward the DR 21(OH) molecular cloud have shown that it is composed of four components. Two of them, designated MM 1 and MM 2, are warm ($T_D = 58$ and 30 K), massive ($M_{TOT} = 350$ and $570 M_{\odot}$), and have associated OH and H_2O maser emission. A source of $20 \mu m$ continuum emission with no associated molecular line or millimeter continuum emission is located to the northeast of MM 1 along the same axis as MM 1 and MM 2 (Genzel 1989). Therefore, within a region $\sim 45,000$ AU in extent we see three phases of early stellar formation: deeply embedded (MM 2), embedded pre-main-sequence (MM 1), and emerged young star (northeastern $20 \mu m$ source). The other two compact sources in the region, designated DR 21(OH)W and DR 21(OH)S, are also warm ($T_D \gtrsim 20$ K), but are less dense than the DR 21(OH) main sources and have no associated OH or H_2O maser emission. Nonetheless, the luminosities of both DR 21(OH)W and DR 21(OH)S identify them as sites of early B star formation. The MM 1/MM 2 and DR 21(OH)S components possess size and luminosity characteristics intermediate between the Ophiuchus molecular core and the Kleinmann-Low nebula of the Orion molecular cloud. DR 21(OH) has formed several embedded massive stars. The observations presented here suggest many more, less massive, cluster members have evaded detection.

J. G. M. would like to thank the National Radio Astronomy Observatory for support through a Junior Research Associateship. We also thank the staff at the Owens Valley Radio Observatory for their assistance with the observations and Neal Evans for helpful comments on the text. This work was supported in part by Texas Advanced Research Program grant 003658-285 and National Science Foundation grant AST-9017710 to the University of Texas.

REFERENCES

- Batra, W., & Menten, K. A. 1988, ApJ, 329, L117
 Campbell, M. F., Hoffmann, W. F., Thronson, H. A., Jr., Niles, D., Nawfel, R., & Hawrylycz, M. 1982, ApJ, 261, 550
 Chakerian, C., & Tipping, R. H. 1983, J. Molec. Spectrosc., 99, 431
 Day, K. L. 1976, ApJ, 210, 614
 Downes, D., & Rinehart, R. 1966, ApJ, 144, 937
 Fischer, J., Sanders, D. B., Simon, M., & Solomon, P. M. 1985, ApJ, 293, 508
 Frerking, M. A., Langer, W. D., & Wilson, R. W. 1982, ApJ, 262, 590
 Garden, R., Geballe, T. R., Gatley, I., & Nadeau, D. 1986, MNRAS, 220, 203
 Gear, W. K., Chandler, C. J., Moore, T. J. T., Cunningham, C. T., & Duncan, W. D. 1988, MNRAS, 231, 47p
 Genzel, R. 1989, private communication

- Genzel, R., & Downes, D. 1977, *A&AS*, 30, 145
 Harris, S. 1973, *MNRAS*, 162, 5p
 Harvey, P. M., Campbell, M. F., & Hoffmann, W. F. 1977, *ApJ*, 211, 786
 Harvey, P. M., Joy, M., Lester, D. F., & Wilking, B. A. 1986, *ApJ*, 300, 737
 Hildebrand, R. H. 1983, *QJRAS*, 24, 267
 Johnston, K. J., Henkel, C., & Wilson, T. L. 1984, *ApJ*, 285, L85
 Koike, C., Hasegawa, H., & Manabe, A. 1980, *A&SS*, 67, 495
 Lane, A. P., Haas, M. R., Hollenbach, D. J., & Erickson, E. F. 1990, *ApJ*, 361, 132
 Mangum, J. G., Wootten, A., & Mundy, L. G. 1991, in preparation
 Mauersberger, R., Henkel, C., Wilson, T. L., & Walmsley, C. M. 1986, *A&A*, 162, 199
 Mauersberger, R., Wilson, T. L., Batrla, W., Walmsley, C. M., & Henkel, C. 1985, *A&A*, 146, 168
 Miller, G. E., & Scalo, J. M. 1979, *ApJS*, 41, 513
 Norris, R. P., Booth, R. S., Diamond, P. J., & Porter, N. D. 1982, *MNRAS*, 201, 191
 Padin, S., et al. 1989, *ApJ*, 337, L45
 Panagia, N. 1973, *AJ*, 78, 929
 Richardson, K. J., Sandell, G., & Krisciunas, K. 1989, *A&A*, 224, 199
 Richardson, K. J., White, G. J., Monteiro, T. S., & Hayashi, S. S. 1988, *A&A*, 198, 237
 Richardson, K. J., White, G. J., Phillips, J. P., & Avery, L. W. 1986, *MNRAS*, 219, 167
 Thum, C., & Lemke, D. 1975, *A&A*, 41, 467
 Tielens, A. G. G. M., & Allamandola, L. J. 1987, in *Interstellar Processes*, ed. D. J. Hollenbach, D. J. & H. M. Thronson, Jr. (Dordrecht: Reidel), 397
 Werner, M. W., Elias, J. H., Gezari, D. Y., Hauser, M. G., & Westbrook, W. E. 1975, *ApJ*, 199, L185
 Werner, M. W., Gatley, I., Harper, D. A., Becklin, E. E., Loewenstein, R. F., Telesco, C. M., & Thronson, H. A. 1976, *ApJ*, 204, 420
 Wilking, B. A. 1989, *PASP*, 101, 229
 Wilking, B. A., & Lada, C. J. 1983, *ApJ*, 274, 698
 Wilking, B. A., Lada, C. J., & Young, E. T. 1989, *ApJ*, 340, 823
 Woody, D. P., Scott, S. L., Scoville, N. Z., Mundy, L. G., Sargent, A. I., Padin, S., Tinney, C. G., & Wilson, C. 1989, *ApJ*, 337, L41
 Wootten, A., Snell, R., & Evans II, N. J. 1980, 240, 532
 Wynn-Williams, C. G., Becklin, E. E., & Neugebauer, G. 1974, *ApJ*, 187, 473